Materials
Horizons

Octahedron rotation evolution in 2D perovskites and its impact on optoelectronic properties: the case of Ba-Zr-S chalcogenides

Journal:	*Materials Horizons*
Manuscript ID	MH-COM-07-2020-001092.R1
Article Type:	Communication
Date Submitted by the Author:	13-Aug-2020
Complete List of Authors:	Chen, Ming; Shanghai Institute of Ceramics Chinese Academy of Sciences, State Key Laboratory of High Performance Ceramics and Superfine Microstructure Yang, Ke; Hunan University, Department of Applied Physics Zeng, Hao; University at Buffalo - The State University of New York, Department of Physics Zhang, Shengbai; Rensselaer Polytechnic Institute, Sun, Yi-Yang; Shanghai Institute of Ceramics Chinese Academy of Sciences, State Key Lab of High Performance Ceramics and Superfine Microstructure

SCHOLARONE™
Manuscripts

Perovskite materials can have self-passivated surfaces without resorting to reconstructions or other passivating agents. This feature renders perovskite materials intrinsically suited for making two-dimensional (2D) materials. Previous studies often considered the structure of 2D perovskites to be directly terminated from the bulk. However, octahedron rotation (OR) being the distinctive structural feature of perovskite materials appears to be an unexplored degree of freedom in 2D. In this work, the OR patterns in 2D perovskites are systematically studied for the first time by employing an adapted Glazer's notation. It is found that as the slab thickness is below several unit cells, the OR pattern deviates from that of the bulk suggesting that the OR is worth attention in future studies on 2D perovskites. From an application point of view, the OR provides a novel tuning knob for enhancing the properties of 2D materials, which is absent in existing 2D materials, such as graphene and transition metal dichalcogenides.

Octahedron rotation evolution in 2D perovskites and its impact on optoelectronic properties: the case of Ba-Zr-S chalcogenides†

Received 00th January 20xx,
Accepted 00th January 20xx

DOI: 10.1039/x0xx00000x

Chen Ming,[a] Ke Yang,[b, c] Hao Zeng,[d] Shengbai Zhang[b] and Yi-Yang Sun*[a]

Octahedron rotation (OR) is a unique structural feature in most perovskite materials. During dimensional reduction from bulk to two-dimensional (2D) perovskites, how the OR pattern evolves is still an open question. Here, we employ an adapted Glazer's notation from bulk perovskites to systematically study the structural evolution of 2D perovskites by fully considering the possible OR patterns. Applying this approach to 2D Ba-Zr-S system, we establish the relation between the OR pattern and slab thickness. It is found that as the thickness decreases, the OR pattern undergoes a transition by suppressing out-of-plane rotations. The OR in 2D chalcogenide perovskites could result in an anti-confinement effect, i.e., reducing the band gap to even below that of the bulk by countering the quantum confinement effect. In addtion, we show that the Ba-Zr-S 2D perovskites exhibit reasonable electron mobility of ~150 cm^2 V^{-1} s^{-1} and large exciton binding energy of ~0.9 eV. Combining the slab thickness and strain as effective knobs for widely tuning the electronic structure, we suggest the 2D chalcogenide perovskites as promising optoelectronic materials.

Introduction

Perovskite materials are well known for dielectric applications owing to their excellent piezoelectric and ferroelectric properties.[1, 2] In recent years, the advent of halide perovskites for photovoltaic and optoelectronic applications has established this old family of materials as semiconductors. The perovskite semiconductors, particularly the halide perovskites, have been found to exhibit unique combinations of optoelectronic properties, such as ultra-long carrier lifetimes[3-5] and extraordinary defect tolerance.[6-9] These exciting findings and their applications in devices have ignited a wave of research in the past several years.[10-13] However, the stability of halide perovskites and the use of lead in these materials have hindered their applications.[11, 14, 15] Alternative perovskites that can mitigate the shortcomings, while preserving the desired properties, of halide perovskites are under intensive research.

Chalcogenide perovskites (CPs) have recently been proposed for photovoltaic applications.[16-18] Also, it has been experimentally demonstrated to exhibit excellent light-emitting properties.[19] Experimental efforts have been made to explore the optical properties of some of the proposed materials.[17, 20, 21] $BaZrS_3$ is one of the promising candidates among CPs for photovoltaic applications, which is air stable, environmental friendly and contains only earth-abundant elements.[17, 20-22] The band gap (E_g) reported for $BaZrS_3$ is from 1.74 to 1.85 eV.[17, 21] Ti-doping has been attempted to further reduce E_g for optimizing solar light absorption.[23] Thin films of $BaZrS_3$ have also been prepared and their electronic and optical properties were reported.[24] With these efforts, CPs are poised to emerge as a new family of semiconductor materials. Ruddlesden-Popper (RP) phase of chalcogenides as a derivative perovskite structure has also been explored for optoelectronic applications.[25-28]

Dimension reduction is a strategy for tuning the material properties. As a material approaches the two-dimensional (2D) limit, the physical properties could be dramatically changed from those of bulk due to quantum confinement effects. Typical examples include graphene and transition metal dichalcogenides (TMDs), which exhibit distinctly different properties compared with their bulk counterpart.[29, 30] Monolayer-thick perovskites were first reported for the halide perovskite $(C_4H_9NH_3)_2PbBr_4$, where an unusual structural relaxation has been observed which leads to a band gap shift as compared to the bulk crystal.[31] More recently, freestanding oxide perovskites as thin as one unit cell have been fabricated and it has been found that $BiFeO_3$ exhibits giant polarization when approaching the monolayer limit.[32] 2D oxide perovskites have also been theoretically predicted to exhibit strongly enhanced ferroelectricity.[33] Before proceeding further, we note that there have been many studies referring to the layered perovskites as "2D perovskites", such as the RP and Dion–Jacobson phase,[34] where perovskite layers periodically stack into bulk structure. But here we define 2D perovskites as thin perovskite slabs bounded by vacuum.

---

[a] State Key Laboratory of High Performance Ceramics and Superfine Microstructure, Shanghai Institute of Ceramics, Chinese Academy of Sciences, Shanghai, 201899, China
[b] Department of Physics, Applied Physics & Astronomy, Rensselaer Polytechnic Institute, Troy, NY, 12180, USA
[c] School of Physics and Electronics, Hunan University, Changsha, 410082, China
[d] Address here. Department of Physics, University at Buffalo, The State University of New York, Buffalo, NY, 14260, USA

† Electronic Supplementary Information (ESI) available: calculation method of dielectric constant, energy profile of Glazer OR patterns, phonon spectrum, formation energy, A-site displacement and band structures of 2D chalcogenide perovskites, and the band structure and band gap evolution of MoS_2 with strain.

2D perovskites are different from the common 2D materials like graphene and TMDs. The latter are derived from layered materials, where interlayer interaction is typically weak van der Waals force so that the 2D structures change little from the bulk. However, bulk perovskite materials are 3D-bonded materials exhibiting more complex structural features, notably octahedron rotation (OR) and symmetry-breaking displacement of transition metal ions within the octahedra. Thus, there is additional structural degree of freedom enhancing the tunability of 2D perovskite properties compared with layered materials through dimension reduction. However, there has been no systematic study on the detailed atomic structures of 2D perovskites with respect to OR pattern, even though atomic structures are usually the starting points for quantitatively studying all other properties.

In this paper, by taking Ba-Zr-S system as a demonstrating example, we show how the atomic structures of 2D perovskites could drastically deviate from bulk perovskites. The approach proposed here is to adapt the Glazer's notation to the 2D perovskites. This notation was developed for classifying the types of ORs in bulk perovskites. With this approach, we are able to systematically evaluate the stability of all possible OR patterns and determine the most stable structure at a given thickness, so that the relation between the OR pattern and the thickness of 2D perovskites can be established. The OR is found to affect the electronic structure of 2D perovskites in a nontrivial way. In addition, strain is found to readily tune the OR. The new understanding on the OR patterns is expected to provide a guidance in the development of 2D perovskites. Meanwhile, the wide tunability of the band gap by thickness and strain, combined with the calculated reasonable electron mobility (~150 cm^2 V^{-1} s^{-1}) and large exciton binding energy (~0.9 eV) renders the 2D chalcogenide perovskites promising optoelectronic materials.

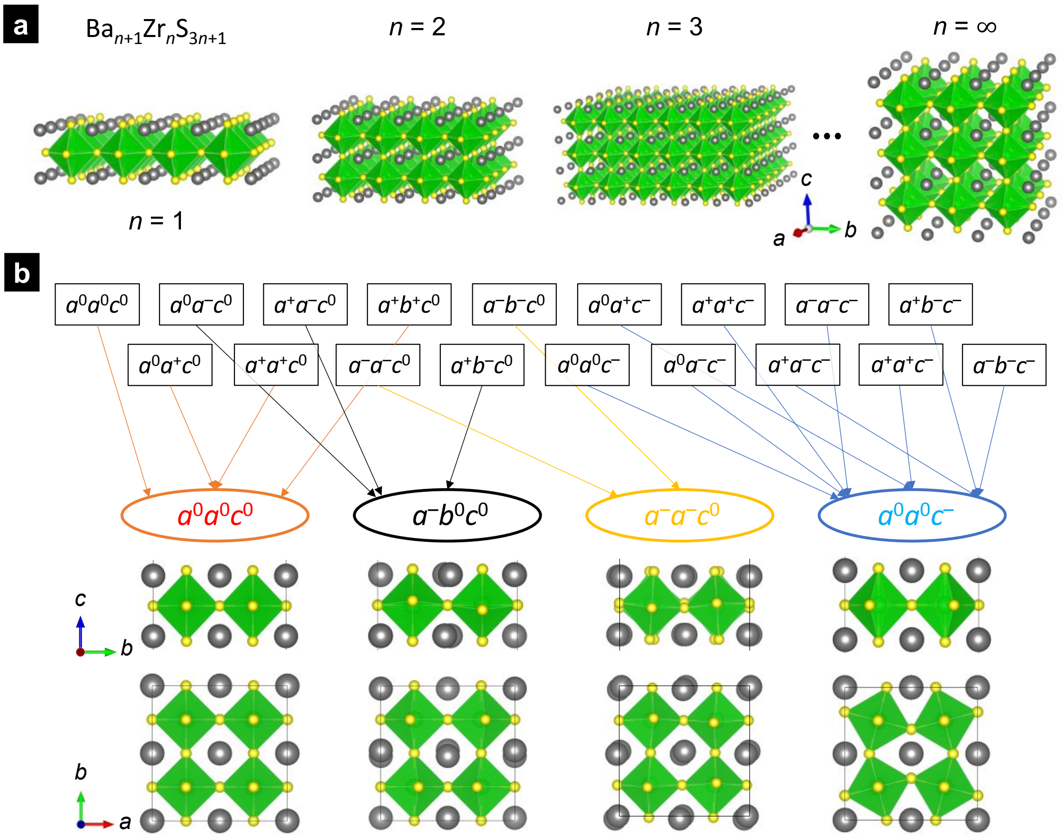

Fig. 1. (a) Atomic structures illustrating the evolution from 2D perovskites to the bulk perovskite. Using the Ba-Zr-S system as an example, the general chemical formula is $Ba_{n+1}Zr_nS_{3n+1}$. (b) 18 octahedron rotation patterns according to an adapted Glazer's notation, which end up with four inequivalent structures after structural relaxation in Ba_2ZrS_4 (n = 1). The lower panels show the side and top views of the optimized structures. Ba, Zr and S atoms are represented by gray, green and yellow spheres.

Results and discussion

Fig. 1(a) illustrates how 2D perovskites evolve into bulk perovskites. Given a general formula of $Ba_{n+1}Zr_nS_{3n+1}$, one can specify the thickness of the 2D perovskite by the integer n. By electron counting, it can be seen that for each n, the 2D perovskite is charge balanced between the cations and anions and, therefore, a semiconductor with the surface self-passivated. This is a property not possessed by traditional group-IV, III-V and II-VI semiconductors, for which the creation of a surface typically introduces dangling bonds. Another distinctive feature of the perovskite structure is the rotational degree of freedom of the octahedra due to their corner-sharing nature as seen in Fig. 1(a). The occurrence of OR is correlated to the Goldschmidt tolerance factor t, defined as

$t = (r_A + r_X)/\sqrt{2}(r_B + r_X)$, where r_A, r_B and r_X are radii of cations A, B and anion X in ABX_3, respectively. Empirically, the perfect perovskite structure holds for t around 1, while OR occurs for $t < 0.95$.[35] For halide (X = Cl, Br and I) and chalcogenide (X= S and Se) perovskites, as the size of constituent anions are large, t is always smaller than 1, thus ORs are ubiquitous in these materials.

It is expected that the OR pattern will be different during the transition from bulk to 2D perovskites. To study this, we employ the Glazer's scheme of classifying the rotation patterns.[36] A main assumption of this scheme is that the period of rotation ordering extends up to two nearest neighbors only. This is valid because no longer period has been reported experimentally. The notation for describing the rotational pattern is as follows: (1) use three letters a, b and c to denote the rotations along the three principal axes and three superscripts to denote the ordering of two neighboring octahedra; (2) if the rotation angles along two or three axes are equal, use the same letter to denote those directions; (3) if the rotation directions of two neighboring octahedra along one direction are the same, a^+ is used for that direction; if opposite, a^- is used; if there is no rotation along that direction, a^0 is used. For bulk perovskites, there are 23 patterns following the Glazer's notation.[36] For 2D perovskites, as the third direction c is inequivalent to the other two directions, there are more rotational freedom than bulk perovskites. For the first two directions, there are 9 patterns, namely, a^0a^0, a^0a^+, a^0a^-, a^+a^+, a^+a^-, a^-a^-, a^+b^+, a^+b^-, and a^-b^-. Combining c^0, c^+, and c^- along the third direction, one has totally 27 possible rotational patterns for a 2D perovskite. Usually, not all of these patterns are stable. After performing structural relaxations, some of them will end up with the same structure.

Fig. 1(b) illustrates the case of 2D Ba_2ZrS_4 (n = 1). Note that for this case, there is only one octahedron layer along the c direction. So, there is no difference between c^- and c^+ patterns and there are only 18 patterns for this case, as displayed in Fig. 1(b). For convenience, we use the label c^- hereafter for the case of n = 1. After structural relaxation using the Perdew-Burke-Ernzerhof (PBE) functional,[37] the 18 OR patterns end up with four, i.e., $a^0a^0a^0$, $a^-b^0c^0$, $a^-a^-c^0$, and $a^0a^0c^-$, as shown in the bottom panels of Fig. 1(b). The energy profile for all the 18 patterns is shown in Fig. S1 (ESI†). We further used the strongly constrained and appropriately normed (SCAN) functional[38] to determine the relative stability of the four structures with higher accuracy. The $a^0a^0c^-$ structure was found to be the most stable one (see Table S1, ESI†). In this structure, there is only one rotation about the c axis, or in-plane rotation. The OR angle is 29.2°, which is evaluated as the deviation of the Zr-S-Zr bond angle from 180°. We carried out the phonon spectrum calculation by the temperature dependent effective potential (TDEP) method[39] and found that this structure is dynamically stable without exhibiting any imaginary modes at room temperature (Fig. S2, ESI†).

The most stable OR pattern for the 2D perovskite $Ba_{n+1}Zr_nS_{3n+1}$ with n = 1 is distinctively different from its bulk counterpart, which has a space group *Pnma* (No. 62) with the $a^-a^-c^+$ pattern. So, we next study the cases of n = 2, 3, 4, and 5 following the same procedure as the case of n = 1, with an aim of establishing the relation between the thickness and the OR pattern. Our results show that for the cases of n = 2 and 3, the most stable structures are $a^0a^0c^-$, the same as the case of n = 1, i.e., only in-plane rotation appears and the relative rotation between neighboring octahedron layers along the c-axis alternates. For the cases of n = 4 and 5, however, the most stable structures are both $a^-a^-c^+$, which is similar to bulk $BaZrS_3$. Clearly, when the thickness of 2D perovskite is reduced to below three octahedron layers, the rotation pattern undergoes a transition, mainly by suppressing the out-of-plane rotations about the a and b axes.

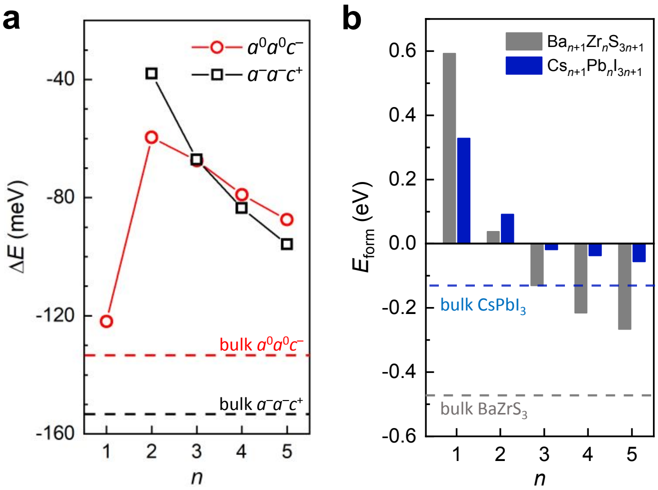

Fig. 2. (a) Relative energy of 2D perovskites $Ba_{n+1}Zr_nS_{3n+1}$ with two of the most relevant octahedron rotation (OR) patterns with respect to that of the ideal structure without OR, calculated as $\Delta E = (E_{OR} - E_{ideal})/n$. The dashed lines denote the values of the bulk perovskites with the two corresponding patterns. (b) Formation energy of the 2D perovskites according to the reaction (n+1) BaS + n ZrS_2 → $Ba_{n+1}Zr_nS_{3n+1}$, calculate as $E_{form} = [E_{2D} - n\,E_{ZrS_2} - (n+1)\,E_{BaS}]/n$, compared with that of 2D halide perovskites $Cs_{n+1}Pb_nI_{3n+1}$ calculated in the same way. The dashed lines denote E_{form} of the bulk perovskites $BaZrS_3$ and $CsPbI_3$ in the *Pnma* phase.

Fig. 2(a) quantitatively shows the stability versus n for two of the most relevant rotation patterns $a^0a^0c^-$ and $a^-a^-c^+$. The stability is evaluated by the relative energy ΔE, calculated as $\Delta E = (E_{OR} - E_{ideal})/n$, where E_{OR} and E_{ideal} are the energy of $Ba_{n+1}Zr_nS_{3n+1}$ in the structures with and without OR, respectively. The normalization of the energy by thickness n allows us to compare the stability of OR patterns for different thickness. Note that the chemical formula $Ba_{n+1}Zr_nS_{3n+1}$ approaches the bulk $BaZrS_3$ when n goes to infinity. According to our calculation for bulk $BaZrS_3$, the most stable structure is $a^-a^-c^+$, in agreement with experimental structure. It is 21 meV lower in energy than $a^0a^0c^-$ (Fig. 2(a)) When the thickness is reduced to n = 5, even though the $a^-a^-c^+$ structure is still the lowest in energy, the difference is reduced to 8 meV. For the case of n = 4, the difference is even smaller. For n = 3, the two structures are nearly degenerate. When n = 1 and 2, the $a^0a^0c^-$ pattern becomes the most stable one.

Fig. 2(b) shows the formation energy (E_{form}) of $Ba_{n+1}Zr_nS_{3n+1}$ for n from 1 to 5 according to the reaction (n+1) BaS + n ZrS_2 → $Ba_{n+1}Zr_nS_{3n+1}$ using the SCAN functional, which reflects the thermodynamic stability. E_{form} is calculated as $E_{form} = [E_{2D} - n\,E_{ZrS_2} - (n + 1)\,E_{BaS}]/n$, where E_{2D}, E_{ZrS_2} and E_{BaS} denote the energy of 2D perovskites and the binary reactants, respectively. It is seen that when thickness decreases, the thermodynamic stability lowers. When $n < 3$, E_{form} turns to be positive. As a comparison, we carried out calculations on 2D halide perovskites $Cs_{n+1}Pb_nI_{3n+1}$ and obtained the same trend as the chalcogenides, as shown in Fig. 2(b). This result further supports the previous conclusion that organic ligands are key to enhance the stability of RP phase hybrid halide perovskites.[40, 41]

Taking BaS and ZrS_2 as a reference in the discussion above is to consider the two materials as the most possible precursors in experimental synthesis. However, it is noted that bulk $BaZrS_3$ is a more competitive phase than the binaries. By considering the reaction $BaS + n\,BaZrS_3 \rightarrow Ba_{n+1}Zr_nS_{3n+1}$, the E_{form} of $Ba_{n+1}Zr_nS_{3n+1}$ is more positive as shown in Fig. S3 (ESI†). For Ba_2ZrS_4 ($n = 1$), E_{form} is 1.06 eV. Considering the dynamical stability as demonstrated by the phonon spectrum at room temperature for Ba_2ZrS_4 (Fig. S2, ESI†), we expect that the 2D chalcogenide perovskites are metastable phases. Non-equilibrium synthesis techniques should be adopted to fabricate these materials, such as growing the 2D layers on a sacrificial substrate, which has recently been used to fabricate freestanding monolayers of oxide perovskites.[32]

With the atomic structures determined, we next studied the effect of OR on the electronic structure of 2D perovskite $Ba_{n+1}Zr_nS_{3n+1}$. The most stable structure for $n = 1$ exhibits a direct band gap at Γ point. For n from 2 to 5, nearly degenerate valence band maxima appear at Γ and M points. The band structures for n = 1, 3, and 5 are shown in Fig. S4 (ESI†). Fig. 3(a) shows the calculated E_g by the SCAN functional as a function of n. A surprising result is that $Ba_{n+1}Zr_nS_{3n+1}$ with two OR patterns both exhibit smaller E_g than that of corresponding bulk when n is greater than 3. As is generally perceived, when the thickness of a semiconductor reduces to below several nanometers, the quantum confinement effect will increase the E_g from the bulk value. To better show the anti-confinement effect observed in Fig. 3(a), we calculated the E_g of bulk-terminated 2D structure (with the $a^-a^-c^+$ pattern) without further relaxation. The results are also shown in Fig. 3(a). It can be seen that these slabs always show larger E_g than the bulk and follow a common trend of quantum confinement effect. This suggests that other than the qualitative OR pattern, quantitative details of OR also play a key role on the electronic structure of these 2D perovskites.

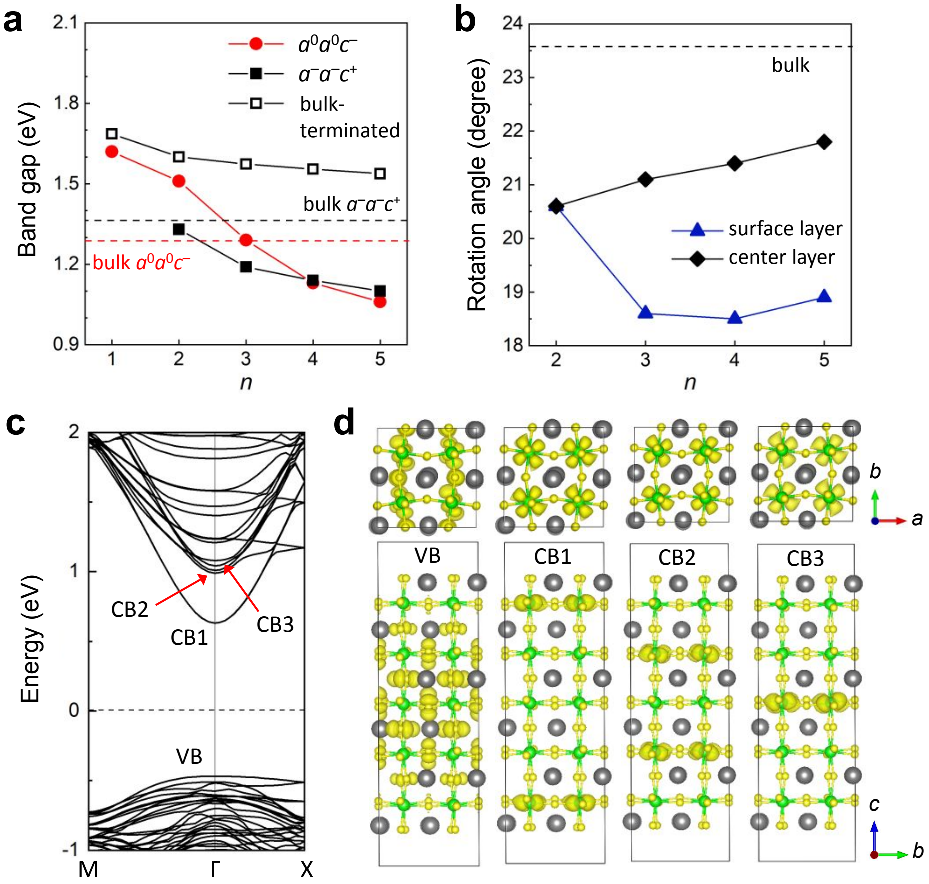

Fig. 3. (a) Band gap of 2D perovskites $Ba_{n+1}Zr_nS_{3n+1}$ calculated using the SCAN functional as a function of thickness for two octahedron rotation patterns and the structures directly cut from the bulk $BaZrS_3$ (with the $a^-a^-c^+$ pattern) without structural relaxation, labelled as “bulk-terminated”. The dashed lines denote the band gaps of bulk $BaZrS_3$ with the two patterns. (b) Evolution of the in-plane octahedron rotation angle within the surface (blue) and the center (black) layers with the thickness n in $Ba_{n+1}Zr_nS_{3n+1}$ (with the $a^-a^-c^+$ pattern). The dashed line denotes the in-plane rotation angle in the bulk. (c) Band structure of $Ba_6Zr_5S_{16}$ ($n = 5$ with the $a^-a^-c^+$ pattern), where VB, CB1, CB2 and CB3 denote the valence band, the first, second and third conduction bands, respectively. Note that both CB1 and CB2 are doubly degenerate. (d) Partial charge density plots of the states denoted in (c) at Γ point. A $\sqrt{2} \times \sqrt{2}$ supercell was used in the calculation of (c) and (d) to better illustrate the interaction of Zr-d orbitals.

We then analyzed the OR angles in the relaxed structures and correlated them with the electronic structures. Fig. 3(b) shows the evolution of the in-plane OR angles in the surface and the center layers as a function of *n* for the $a^-a^-c^+$ pattern. We observed that the relaxed structures exhibit a non-uniform in-plane OR angle distribution, i.e., the OR angle is strongly layer dependent and it is significantly reduced in the surface layer. For the case of $n = 5$, the OR angle in the surface layer is suppressed to below 19° compared with 22° in the center layer, while the OR angle is 23.6° in bulk. We analyzed the detailed electronic structures and show the band structure and charge density plots for the case of $n = 5$ in Figs. 3(c) and (d), respectively. As can be seen in Fig. 3(d), the conduction bands are mainly composed of the in-plane Zr-*d* orbitals, the suppressed in-plane OR enhances the overlap between these orbitals and leads to the more dispersed conduction bands, as shown in Fig. 3(c), and the reduced band gap. We thus attribute the anti-confinement effect in Fig. 3(a) to the OR suppression in the surface.

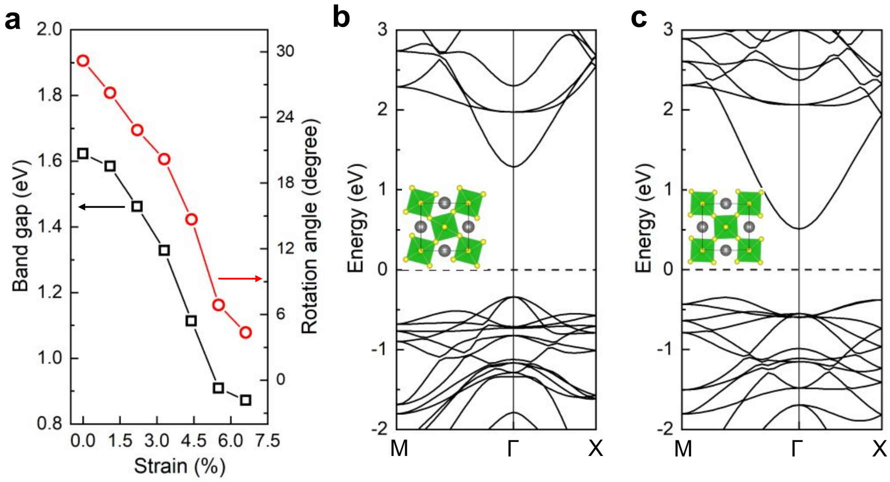

Fig. 4. (a) Band gap of Ba_2ZrS_4 ($n = 1$) as a function of the applied biaxial strain. The evolution of octahedron rotation angle with strain is also shown. Band structures of Ba_2ZrS_4 at zero (b) and 6.6% strain (c). The insets are the top views of the corresponding atomic structures.

The OR is usually accompanied by displacements of A-site atoms as found in bulk chalcogenide perovskites and RP phases,[28] where the atoms in adjacent layers shift in opposite directions along the pseudo-cubic [110] direction, as illustrated in Fig. S5 (ESI†). This displacement has been proposed to induce ferroelectricity in the RP phase.[28] We found that such A-site displacement also exists in 2D perovskite $Ba_{n+1}Zr_nS_{3n+1}$ with $a^-a^-c^+$ pattern, but the magnitude is reduced compared with bulk. As shown in Fig. S5 (ESI†), the magnitude of displacement is smaller in the surface layer compared with inner layers. With the thickness increasing, the magnitude in the inner layers increases toward that of the bulk, while on the surface it remains small. Such trend of displacement is similar to that of OR angle in Fig. 3(b), suggesting that the A-site displacement is still correlated to the OR with the $a^-a^-c^+$ pattern. We also checked the $a^0a^0c^-$ pattern, but did not find such displacement.

To further demonstrate the effect of OR, we use strain as a tuning knob to control the OR by taking the monolayer Ba_2ZrS_4 as an example. Fig. 4(a) shows the E_g and the in-plane OR angle as a function of the biaxial strain. As the strain increases, the OR angle decreases. When the strain is greater than about 7%, the OR nearly vanishes. E_g decreases monotonically with the suppression of OR and roughly follows a quadratic relationship with the strain when the strain is below 6%. A transition occurs at about 6% strain, where the band gap changes from a direct to an indirect gap. The band structures at zero and 6.6% strain are shown in Figs. 4(b) and (c), respectively. It can be seen that when the strain increases, there is a second peak in the path from Γ to M point rises as new valence band maximum. The strain effect on E_g is relatively large. The direct gap decreases by 0.71 eV when strain increases to 5.5%, which is about a 44% reduction from the value without strain. As a comparison, we found the reduction of the direct gap in MoS_2 is only 0.52 eV (about 30% reduction) at the same strain condition. The 2D chalcogenide perovskites are relatively soft materials compared with TMDs, such as MoS_2. We calculated the 2D elastic modulus by $C_{2D}=(1/A)\partial^2E/\partial\varepsilon^2$, where *A* is the area of the unit cell, *E* the total energy and ε the strain. For the case of $n = 1$, C_{2D} is calculated to be 71 J/m^2, while it is 141 J/m^2 for MoS_2. Owing to the large variation of E_g with strain as shown in Fig. 4(a) and the small Young's modulus, $Ba_{n+1}Zr_nS_{3n+1}$ is expected to exhibit large tunability of the band gap through either mechanical stress or epitaxial stress from substrates.

The direct band gap and its wide tunability due to either thickness or strain suggest that the 2D perovskites $Ba_{n+1}Zr_nS_{3n+1}$ be potential optoelectronic materials. We therefore studied the carrier mobility and excitonic property, which are the quantities of interest for optoelectronic applications by taking the monolayer Ba_2ZrS_4 as an example. We applied two models to evaluate the mobility according to different mechanisms. The first one is the widely used deformation potential model[42-44]. It assumes that the mobility is limited by scattering of longitudinal acoustic phonons, and the strength of electron-phonon interaction is described by the deformation potential. Then the mobility denoted as μ_{DP} is determined by the effective mass (m^*), deformation potential (E_1) and elastic modulus. As shown in Table 1, the effective mass of electrons in monolayer Ba_2ZrS_4 is 0.22 m_0, which is much smaller than that of MoS_2 (0.4 m_0), while its hole effective mass is 0.5 m_0. The effective mass is found to be isotropic as m^* along Γ-X and Γ-M are similar, indicating isotropic transport in this material. The predicted μ_{DP} of electrons reaches ~1000 cm^2 V^{-1} s^{-1} (Table 1), while the hole mobility is relatively low due to the large m^* and E_1.

Table 1 The parameters and predicted carrier mobility of Ba_2ZrS_4 at room temperature based on two models.

Deformation potential model:

	m^*/m_0	C_{2D} (J m^{-2})	E_1 (eV)	μ_{DP} (cm^2 V^{-1} s^{-1})
e	0.22	71	5.4	1071
h	0.50	71	6.3	152

Polaron model:

	ε^∞	ε^0	Ω (THz)	$\mu_{polaron}$ (cm^2 V^{-1} s^{-1})
e	11.4	65.3	0.81	151
h	11.4	65.3	0.81	41

It is known that in ionic semiconductors the interaction of the longitudinal optical (LO) phonons with carriers could strongly affect the carrier mobility.[45, 46] This interaction may lead to the formation of large polarons and reduce carrier mobility as found in halide perovskites.[46, 47] To consider this effect, we used the refined Hellwarth polaron model[46, 48] to evaluate the mobility in Ba_2ZrS_4, denoted by $\mu_{polaron}$. In this model, the mobility is determined by high-frequency and static dielectric constants (ε^∞ and ε^0), LO frequency (Ω) and effective mass (m^*). As shown in Table 1, the calculated in-plane ε^∞ and ε^0 are 11.4 and 65.3, respectively, which are larger than that of halide perovskites, e.g. 5.0 and 33.5 for $CH_3NH_3PbI_3$.[47] The large difference between ε^∞ and ε^0 suggests that the LO phonon modes dominate the low-frequency dielectric response in this material, exhibiting strong interaction with carriers. The predicted $\mu_{polaron}$ are 151 and 41 cm^2 V^{-1} s^{-1} for electrons and holes, respectively (Table 1). These values are significantly smaller compared with μ_{DP} (1071 and 152 cm^2 V^{-1} s^{-1}) indicating that the LO phonons are dominant in this material over the acoustic phonons. The predicted electron mobility is comparable to that of halides perovskites (~100 cm^2 V^{-1} s^{-1})[49] while smaller than that of MoS_2 (<400 cm^2 V^{-1} s^{-1}).[50]

The exciton binding energy (E_b) of monolayer Ba_2ZrS_4 is calculated based on *ab initio* G_0W_0[51] method and Bethe-Salpeter equation (BSE).[52] As shown in Fig. 5(a), compared with dielectric constant from random phase approximation (RPA) excluding excitonic effect, BSE calculation shows that E_b of the lowest exciton is 0.9 eV. This is an unexpectedly large value. As a comparison, the E_b of TMD materials is usually on the order of 0.5 eV.[53] The large E_b is partly due to the large quasiparticle E_g of 3.0 eV, as obtained from the G_0W_0 band structure shown in Fig. 5(b). However, even considering the common 1/4-rule on the relation between E_g and E_b as observed in 2D materials,[53] 0.9 eV is still relatively large. Wave function analysis in the reciprocal space (Fig. 5(c)) shows that the lowest exciton is contributed by the hole and electron at the Γ point confirming the direct band gap. The exciton wave function in real space also suggests the large binding energy in this material, as the size of exciton is only about 2 nm which is much smaller than that of 5 nm in TMD.[54] In addition to the strong exciton effect, the G_0W_0-correction on the E_g of 1.6 eV obtained from the PBE calculation suggests that self-energy effect is also important in this material.

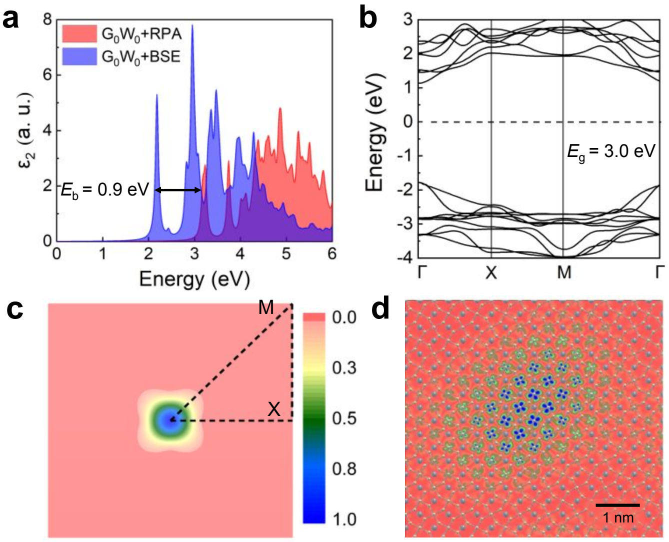

Fig. 5. Quasiparticle properties of Ba_2ZrS_4 (n = 1). (a) Imaginary part of dielectric function (ε_2) based on G_0W_0+RPA (without excitonic effect) and G_0W_0+BSE (with excitonic effect) calculations. (b) Quasiparticle band structure from PBE+G_0W_0 calculation. Wave function of the lowest exciton in reciprocal (c) and real (d) space.

Conclusions

We studied the structure of the 2D perovskites with a focus on the OR patterns and their effects on the electronic structures by taking $Ba_{n+1}Zr_nS_{3n+1}$ as an example. We proposed an approach by adapting the Glazer's notation to systematically study the evolution of OR pattern with the slab thickness. It is found that when the thickness is below three octahedron layers, the rotation pattern transits from the mixed in-plane and out-of-plane rotation pattern to the simpler in-plane rotation pattern. The OR is found to give rise to an anti-confinement effect, which

This journal is © The Royal Society of Chemistry 20xx

could reduce the band gap of $Ba_{n+1}Zr_nS_{3n+1}$ to even below that of the bulk. We also show that the strain can widely tune the OR angle and thus the band gap. Our calculations show that $Ba_{n+1}Zr_nS_{3n+1}$ exhibit reasonable electron mobility and large exciton binding energy suggesting for promising optoelectronic applications. The adapted Glazer's approach proposed here could also be used for systematiccally studying the atomic structures of other 2D perovskites.

Method

Our first-principles calculation was based on the density functional theory (DFT) as implemented in the VASP program.[55] To consider possible OR patterns for each thickness, we followed the Glazer's scheme[36] to construct the initial 2×2×1 supercells of the perfect perovskite structure with various OR patterns. A vacuum region of ~12 Å was used to separate the slabs. We first used the PBE functional[37] to obtain the possible metastable structures. Then, the more accurate SCAN functional[38] was used to further relax the metastable structures. The band structure and effective mass calculations were also based on the SCAN functional. Projector augmented wave (PAW) potentials were used to describe the core−valence interaction.[56] Planewaves with kinetic energy up to 408 eV were used as the basis set. The atomic structures were relaxed until the residual forces on all atoms were smaller than 0.005 eV/Å. Γ-centered 3×3×1 and 6×6×1 k-point grids were used for the structural relaxation and electronic structure calculations, respectively. To calculate the formation energy of 2D halide perovskite $Cs_{n+1}Pb_nI_{3n+1}$, the structures were optimized based on the most stable OR pattern of $Ba_{n+1}Zr_nS_{3n+1}$ for each n. The small energy difference between different OR pattern would not change the trend in Fig. 2(b). Γ-centered 3×3×1 and 6×6×1 k-point grids and SCAN functional were used for the structural relaxation and energy calculations, respectively. The atomic structure, band structure and effective mass of MoS_2 were calculated based on the SCAN functional. Γ-centered 8×8×1 and 19×19×1 k-point grids were used for structural relaxation and electronic calculations, respectively.

The phonon spectrum of the most stable structure of Ba_2ZrS_4 was calculated by the TDEP method.[39] *Ab initio* molecular dynamic simulation with an *NVT* ensemble at 300 K was performed by VASP. A 2×2×1 supercell containing 56 atoms was used. The SCAN functional was used in the simulation. The Γ point and a cutoff energy of 300 eV were used. The simulation was run for 60 ps with a time step of 2 fs. The force constants were extracted from the simulation of the last 50 ps.

The mobility by deformation potential model is[42-44]

$$\mu_{\mathrm{DP}} = \frac{e\hbar^3 C_{2D}}{k_B T m^* m_d E_1^2} \#(1)$$

where m^* is the effective mass along the transport direction, m_d is the density-of-state effective mass defined as $m_d = \sqrt{m_x m_y}$, E_1 is the deformation potential and C_{2D} is the elastic modulus. E_1 is defined as $E_1 = \Delta V/(\Delta l/l)$, where ΔV is the energy shift of valence band maximum (conduction band maximum) for hole (electron), and $\Delta l/l$ is the strain along the transport direction.

The mobility by refined Hellwarth polaron model is[46, 48]

$$\mu_{\mathrm{polaron}} = \left(\frac{w}{v}\right)^3 \frac{3e\sqrt{\pi}\sinh(\beta/2)}{m^* \Omega\alpha\beta^{\frac{5}{2}}} K^{-1} \#(2)$$

where m^* is the effective mass, Ω is the LO frequency, β is $\hbar\Omega/k_B T$, α is the Frölich parameter of dielectric electron-phonon coupling which is determined by the dielectric constants, LO frequency and effective mass. The detailed expression of α, w, v and K can be found elsewhere.[46] The lowest frequency of LO phonons (0.81 THz) was used as Ω.

The dielectric constants and LO phonon frequency were calculated using density functional perturbation theory (DFPT) as implemented in VASP based on PBE functional. Γ-centered 11×11×1 and 6×6×1 k-point grids were used for the calculation of high-frequency and static dielectric constants, respectively. An exaction procedure was further used to obtain the intrinsic dielectric constants for the 2D slab (see details in ESI†).

The G_0W_0[51] and Bethe-Salpeter Equation (BSE)[52] calculations were performed using the YAMBO package.[57] Ground state electronic structures obtained by the Quantum ESPRESSO package[58] were used as the start for many-body calculations. Optimized norm-conserving pseudopotentials[59] were employed with a plane-wave cutoff energy of 816 eV. For the exchange and correlation parts of the self-energy, we used the energy cutoffs of 680 and 136 eV, respectively. A Γ-centered 6×6×1 k-point grid was used for calculating self-energy corrections and dielectric function. 1200 bands were used to ensure converged band gap. Excitonic properties and dielectric function were obtained by solving the BSE based on G_0W_0 results with top 10 valence bands and bottom 10 conduction bands. The truncated coulomb potential technique[60] was used to eliminate the interaction between the repeated images along the non-periodic direction.

Conflicts of Interest

The authors declare no competing financial interest.

Acknowledgements

Y.-Y.S. acknowledges support from National Key Research and Development Program of China under Grant No. 2019YFE0103500 and National Natural Science Foundation of China under Grant No. 11774365. C.M. acknowledges support from Natural Science Foundation of Shanghai under Grant No. 19ZR1421800 and Science Foundation for Youth Scholar of State Key Laboratory of High Performance Ceramics and Superfine Microstructures under Grant No. SKL 201804. H.Z. acknowledges support from U.S. NSF under Grant Nos. CBET-1510121 and CBET-1510948. K.Y. and S.Z. acknowledge support from U.S. DOE under Grant No. DE-SC0002623. The supercomputer time sponsored by National Energy Research Scientific Center (NERSC) under U.S. DOE Contract No. DE-AC02-05CH11231 and the Center for Computational Innovations (CCI) at Rensselaer Polytechnic Institute are also acknowledged.

References

1. B. Jaffe, W. R. Cook and H. Jaffe, *Piezoelectric Ceramics*, Academic, London, 1971.
2. S. Zhang, F. Li, X. Jiang, J. Kim, J. Luo and X. Geng, *Progress in Materials Science*, 2015, **68**, 1-66.
3. S. D. Stranks, G. E. Eperon, G. Grancini, C. Menelaou, M. J. P. Alcocer, T. Leijtens, L. M. Herz, A. Petrozza and H. J. Snaith, *Science*, 2013, **342**, 341-344.
4. D. Bi, W. Tress, M. I. Dar, P. Gao and A. Hagfeldt, *Science Advances*, 2016, **2**, e1501170.
5. M. Saliba, T. Matsui, K. Domanski, J.-Y. Seo, A. Ummadisingu, S. M. Zakeeruddin, J.-P. Correa-Baena, W. R. Tress, A. Abate, A. Hagfeldt and M. Grätzel, *Science*, 2016, **354**, 206-209.
6. W.-J. Yin, T. Shi and Y. Yan, *Advanced Materials*, 2014, **26**, 4653-4658.
7. M. L. Agiorgousis, Y.-Y. Sun, H. Zeng and S. Zhang, *Journal of the American Chemical Society*, 2014, **136**, 14570-14575.
8. J. M. Ball and A. Petrozza, *Nature Energy*, 2016, **1**, 16149.
9. D. Meggiolaro and F. De Angelis, *ACS Energy Letters*, 2018, **3**, 2206-2222.
10. J.-P. Correa-Baena, M. Saliba, T. Buonassisi, M. Grätzel, A. Abate, W. Tress and A. Hagfeldt, *Science*, 2017, **358**, 739-744.
11. M. V. Kovalenko, L. Protesescu and M. I. Bodnarchuk, *Science*, 2017, **358**, 745-750.
12. M. A. Green, A. Ho-Baillie and H. J. Snaith, *Nature Photonics*, 2014, **8**, 506-514.
13. Q. A. Akkerman, G. Raino, M. V. Kovalenko and L. Manna, *Nature materials*, 2018, **17**, 394-405.
14. J. A. Christians, P. A. M. Herrera and P. V. Kamat, *Journal of the American Chemical Society*, 2015, **137**, 1530-1538.
15. B. Conings, J. Drijkoningen, N. Gauquelin, A. Babayigit, J. D'Haen, L. D'Olieslaeger, A. Ethirajan, J. Verbeeck, J. Manca and E. Mosconi, *Advanced Energy Materials*, 2015, **5**, 1500477.
16. Y. Y. Sun, M. L. Agiorgousis, P. Zhang and S. Zhang, *Nano Letters*, 2015, **15**, 581-585.
17. S. Perera, H. Hui, C. Zhao, H. Xue, F. Sun, C. Deng, N. Gross, C. Milleville, X. Xu, D. F. Watson, B. Weinstein, Y.-Y. Sun, S. Zhang and H. Zeng, *Nano Energy*, 2016, **22**, 129-135.
18. M.-G. Ju, J. Dai, L. Ma and X. C. Zeng, *Advanced Energy Materials*, 2017, **7**, 1700216.
19. K. Hanzawa, S. Iimura, H. Hiramatsu and H. Hosono, *Journal of the American Chemical Society*, 2019, **141**, 5343-5349.
20. N. Gross, Y.-Y. Sun, S. Perera, H. Hui, X. Wei, S. Zhang, H. Zeng and B. A. Weinstein, *Physical Review Applied*, 2017, **8**, 044014.
21. S. Niu, H. Huyan, Y. Liu, M. Yeung, K. Ye, L. Blankemeier, T. Orvis, D. Sarkar, D. J. Singh, R. Kapadia and J. Ravichandran, *Advanced Materials*, 2017, **29**, 1604733.
22. S. Niu, J. Milam-Guerrero, Y. Zhou, K. Ye, B. Zhao, B. C. Melot and J. Ravichandran, *Journal of Materials Research*, 2018, **33**, 4135.
23. W. Meng, B. Saparov, F. Hong, J. Wang, D. B. Mitzi and Y. Yan, *Chemistry of Materials*, 2016, **28**, 821-829.
24. X. Wei, H. Hui, C. Zhao, C. Deng, M. Han, Z. Yu, A. Sheng, P. Roy, A. Chen, J. Lin, D. F. Watson, Y.-Y. Sun, T. Thomay, S. Yang, Q. Jia, S. Zhang and H. Zeng, *Nano Energy*, 2020, **68**, 104317.
25. S. Niu, D. Sarkar, K. Williams, Y. Zhou, Y. Li, E. Bianco, H. Huyan, S. B. Cronin, M. E. McConney, R. Haiges, R. Jaramillo, D. J. Singh, W. A. Tisdale, R. Kapadia and J. Ravichandran, *Chemistry of Materials*, 2018, **30**, 4882-4886.
26. Y. Li and D. J. Singh, *The European Physical Journal B*, 2018, **91**, 188.
27. W. Li, S. Niu, B. Zhao, R. Haiges, Z. Zhang, J. Ravichandran and A. Janotti, *Physical Review Materials*, 2019, **3**, 101601.
28. H. Wang, G. Gou and J. Li, *Nano Energy*, 2016, **22**, 507-513.
29. K. S. Novoselov, A. K. Geim, S. V. Morozov, D. Jiang, Y. Zhang, S. V. Dubonos, I. V. Grigorieva and A. A. Firsov, *Science*, 2004, **306**, 666-669.
30. B. Radisavljevic, A. Radenovic, J. Brivio, V. Giacometti and A. Kis, *Nature Nanotechnology*, 2011, **6**, 147-150.
31. L. Dou, A. B. Wong, Y. Yu, M. Lai, N. Kornienko, S. W. Eaton, A. Fu, C. G. Bischak, J. Ma, T. Ding, N. S. Ginsberg, L.-W. Wang, A. P. Alivisatos and P. Yang, *Science*, 2015, **349**, 1518-1521.
32. D. Ji, S. Cai, T. R. Paudel, H. Sun, C. Zhang, L. Han, Y. Wei, Y. Zang, M. Gu, Y. Zhang, W. Gao, H. Huyan, W. Guo, D. Wu, Z. Gu, E. Y. Tsymbal, P. Wang, Y. Nie and X. Pan, *Nature*, 2019, **570**, 87-90.
33. J. Lu, W. Luo, J. Feng and H. Xiang, *Nano Lett*, 2018, **18**, 595-601.
34. L. L. Mao, C. C. Stoumpos and M. G. Kanatzidis, *Journal of the American Chemical Society*, 2019, **141**, 1171-1190.
35. A. F. Wells, *Structural Inorganic Chemistry*, Oxford Science publication, London, 1995.
36. A. Glazer, *Acta Crystallographica Section B*, 1972, **28**, 3384-3392.
37. J. P. Perdew, J. A. Chevary, S. H. Vosko, K. A. Jackson, M. R. Pederson, D. J. Singh and C. Fiolhais, *Physical Review B*, 1992, **46**, 6671-6687.
38. J. Sun, A. Ruzsinszky and J. P. Perdew, *Physical Review Letters*, 2015, **115**, 036402.
39. O. Hellman, I. A. Abrikosov and S. I. Simak, *Physical Review B*, 2011, **84**, 180301.
40. L. N. Quan, M. Yuan, R. Comin, O. Voznyy, E. M. Beauregard, S. Hoogland, A. Buin, A. R. Kirmani, K. Zhao, A. Amassian, D. H. Kim and E. H. Sargent, *Journal of the American Chemical Society*, 2016, **138**, 2649-2655.
41. Y. Jiang, J. Yuan, Y. Ni, J. Yang, Y. Wang, T. Jiu, M. Yuan and J. Chen, *Joule*, 2018, **2**, 1356-1368.
42. S. Takagi, A. Toriumi, M. Iwase and H. Tango, *IEEE Transactions on Electron Devices*, 1994, **41**, 2357-2362.
43. S. Bruzzone and G. Fiori, *Applied Physics Letters*, 2011, **99**, 222108.
44. J. Qiao, X. Kong, Z.-X. Hu, F. Yang and W. Ji, *Nature communications*, 2014, **5**, 4475.
45. L. Cheng and Y. Liu, *Journal of the American Chemical Society*, 2018, **140**, 17895-17900.
46. J. M. Frost, *Physical Review B*, 2017, **96**, 195202.
47. M. Sendner, P. K. Nayak, D. A. Egger, S. Beck, C. Müller, B. Epding, W. Kowalsky, L. Kronik, H. J. Snaith, A. Pucci and R. Lovrinčić, *Materials Horizons*, 2016, **3**, 613-620.
48. R. W. Hellwarth and I. Biaggio, *Physical Review B*, 1999, **60**, 299-307.
49. T. M. Brenner, D. A. Egger, A. M. Rappe, L. Kronik, G. Hodes and D. Cahen, *The Journal of Physical Chemistry Letters*, 2015, **6**, 4754-4757.
50. K. Kaasbjerg, K. S. Thygesen and K. W. Jacobsen, *Physical Review B*, 2012, **85**, 115317.
51. M. S. Hybertsen and S. G. Louie, *Physical Review B* 1986, **34**, 5390-5413.
52. M. Rohlfing and S. G. Louie, *Physical Review B*, 2000, **62**, 4927-4944.
53. Z. Jiang, Z. Liu, Y. Li and W. Duan, *Physical Review Letters*, 2017, **118**, 266401.
54. M. M. Ugeda, A. J. Bradley, S.-F. Shi, F. H. da Jornada, Y. Zhang, D. Y. Qiu, W. Ruan, S.-K. Mo, Z. Hussain, Z.-X. Shen, F. Wang, S. G. Louie and M. F. Crommie, *Nature Materials*, 2014, **13**, 1091-1095.

55. G. Kresse and J. Furthmüller, *Computational Materials Science*, 1996, **6**, 15-50.
56. G. Kresse and D. Joubert, *Physical Review B*, 1999, **59**, 1758-1775.
57. X. Ren, P. Rinke, V. Blum, J. Wieferink, A. Tkatchenko, A. Sanfilippo, K. Reuter and M. Scheffler, *New Journal of Physics*, 2012, **14**, 053020.
58. P. Giannozzi, S. Baroni, N. Bonini, M. Calandra, R. Car, C. Cavazzoni, D. Ceresoli, G. L. Chiarotti, M. Cococcioni and I. Dabo, *Journal of Physics: Condensed Matter*, 2009, **21**, 395502.
59. D. R. Hamann, *Physical Review B*, 2013, **88**, 085117.
60. S. Ismail-Beigi, *Physical Review B*, 2006, **73**, 233103.

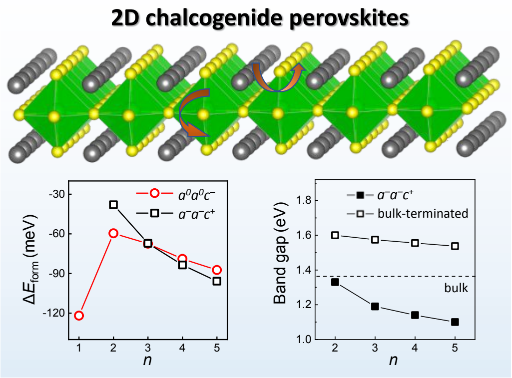

Octahedron rotation as a distinctive structural feature with its impact on opto-electronic properties is systematically studied in 2D chalcogenide perovskites.